

Article

Stage-Specific Benchmarking of Deep Learning Models for Glioblastoma Follow-Up MRI

Wenhao Guo and Golrokh Mirzaei *

Department of Computer Science and Engineering, The Ohio State University, Columbus, USA

Abstract

Differentiating true tumor progression (TP) from treatment-related pseudoprogression (PsP) in glioblastoma remains challenging, especially at early follow-up. We present the first stage-specific, cross-sectional benchmarking of deep learning models for follow-up MRI using the Burdenko GBM Progression cohort ($n = 180$). We analyze different post-RT scans independently to test whether architecture performance depends on timepoint. Eleven representative DL families (CNNs, LSTMs, hybrids, transformers, and selective state-space models) were trained under a unified, QC-driven pipeline with patient-level cross-validation. Across both stages, accuracies were comparable (~ 0.70 – 0.74), but discrimination improved at the second follow-up, with F1 and AUC increasing for several models, indicating richer separability later in the care pathway. A Mamba+CNN hybrid consistently offered the best accuracy–efficiency trade-off, while transformer variants delivered competitive AUCs at substantially higher computational cost and lightweight CNNs were efficient but less reliable. Performance also showed sensitivity to batch size, underscoring the need for standardized training protocols. Notably, absolute discrimination remained modest overall, reflecting the intrinsic difficulty of TP vs. PsP and the dataset’s size/imbalance. These results establish a stage-aware benchmark and motivate future work incorporating longitudinal modeling, multi-sequence MRI, and larger multi-center cohorts.

Keywords: Glioblastoma; MRI; Deep Learning; True Tumor; Pseudoprogression

Academic Editor(s): Name

Received: date

Revised: date

Accepted: date

Published: date

Citation: Guo, W.; Mirzaei, G. Stage-Specific Benchmarking of Deep Learning Models for Glioblastoma Follow-Up MRI. *Cancers* **2025**, *17*, x. <https://doi.org/10.3390/xxxxx>

Copyright: © 2025 by the authors. Submitted for possible open access publication under the terms and conditions of the Creative Commons Attribution (CC BY) license (<https://creativecommons.org/licenses/by/4.0/>).

1. Introduction

Gliomas are a heterogeneous group of tumors that originate from glial cells in the central nervous system and are among the most common types of brain tumors. They account for approximately 30% of all brain tumors and about 80% of malignant brain tumors. Gliomas can be classified into different types, including astrocytomas, oligodendrogliomas, and glioblastomas, with glioblastoma being the most aggressive and lethal form. The prognosis for patients with glioblastoma remains poor, with a median survival of approximately 15 months despite advances in treatment. The complexity and variability of gliomas, coupled with their infiltrative nature, present significant challenges in diagnosis and treatment, underscoring the need for innovative approaches to improve patient outcomes. A critical challenge in the treatment of brain tumors is differentiating between True Tumor Progression (TP) and Treatment Effect (TE), such as pseudo-progression (PsP) and radiation necrosis. TP refers to the actual growth or recurrence of the tumor, indicating a need for a change in treatment strategy to more aggressive or alternative therapies.

In contrast, PsP or radiation necrosis are phenomena related to treatment effects and often managed by close monitoring rather than aggressive treatment. Because their imaging appearances can closely mimic true progression, accurate differentiation is difficult and can complicate clinical decision-making.

Machine learning (ML) and deep learning (DL) methods have been increasingly applied to address this challenge. Hu et al. (2011) applied a support vector machine on multiparametric MRI, comprising diffusion and perfusion parameters. While the study was limited by a relatively small cohort, their voxel-wise classification approach demonstrated that the integration of advanced MRI modalities enhances discriminative ability. Radiomics-based approaches have also shown promise: a random forest classifier trained on T1CE images outperformed neuroradiologists (Sun et al., 2021), gradient boosting on pre-treatment T1CE radiomics demonstrated strong accuracy in external validation (Yadav et al., 2022), and even low-parameter supervised methods yielded moderate AUCs on limited datasets (Warner et al., 2023). Building on these early efforts, deep learning frameworks have achieved significant progress. Early studies combined MRI with clinical data in CNN–LSTM frameworks, achieving improved predictive accuracy over unimodal methods (Jang et al., 2018). Li et al. (2019) proposed a DCGAN–AlexNet framework to mitigate overfitting in small datasets, while CNN–LSTM models treating multi-parametric MRI as spatial sequences further boosted accuracy and AUC (Lee et al., 2020). Automated DL methods such as 3D DenseNet-121 applied to T2 and CET1 MRI (Moassefi et al., 2022), and radiomics classifiers validated on biopsy-proven gliomas (Turk et al., 2022), confirmed the feasibility of noninvasive PsP–TP prediction. Recent work has moved toward advanced multimodal and transformer-based approaches. Integration of imaging features with MGMT promoter methylation achieved high diagnostic performance (Li et al., 2021; McKenney et al., 2022). Multiparametric MRI combined with MGMT status has enhanced PsP–TP classification (Yadav et al., 2024). CFINet, an attention-based cross-modality feature interaction network leveraging T1- and T2-weighted MRI, demonstrated strong generalization on independent cohorts by effectively capturing complementary information across modalities (Lv et al., 2025). Self-supervised multimodal ViTs leveraging contrastive and context-restoration pretraining have further improved performance (Gomaa et al., 2024). Nonetheless, most methods remain constrained to single timepoints and heterogeneous datasets, limiting reproducibility and generalizability.

One of the main challenges in the ML/DL in this setting is the small sample size and resulting class imbalance due to the low prevalence of TP and PsP. Several studies have used oversampling techniques such as SMOTE (Liu et al., 2017). Two-network architectures with similarity loss improved robustness under limited-data conditions (Kalata et al., 2024) by training two identical networks in parallel with independently undersampled k-space inputs at different reduction factors. A cosine similarity-based loss combined with L1 loss enforced the networks to learn both common and distinct features, while exponential moving average (EMA) updating of the target network further stabilized training. Methodological cautions highlight that oversampling must be confined to training sets to avoid data leakage (Demircioğlu, 2024). More advanced methods, such as OCH-SMOTE (Wang & Awang, 2025), DR-SMOTE (Gong et al., 2025), and hybrid BSGAN (Ahsan et al., 2025), have further expanded applicability. Taken together, these findings underscore the importance of class balancing strategies in ensuring robust and generalizable ML/DL pipelines for PsP–TP classification.

Another challenge is how different DL architectures perform across longitudinal follow-ups. Multiple studies have shown that pseudoprogression tends to occur early after radiotherapy, e.g., up to 50% of malignant glioma patients show evidence of pseudo-progression on MRI immediately after chemoradiotherapy (Taal et al., 2008) and about 60% of PsP cases are reported within the first 3 months post-radiotherapy (Taylor et al., 2022).

By contrast, true tumor progression generally emerges later, and MRI changes beyond 3–6 months are more likely to reflect actual recurrence than transient treatment effects (Blakstad et al., 2023). No prior study has systematically examined whether specific architectures are better suited for early versus late follow-ups—a question with direct clinical relevance.

In this work, we address this critical gap using the Burdenko Glioblastoma Progression Dataset (Zolotova et al., 2023), which comprises 180 patients, substantially larger than previously reported cohorts, and provides longitudinal T1C MRI follow-ups. Table 1 summarizes prior studies, where most datasets ranged between 30 and 130 patients. We pre-processed raw MRI data, mitigated class imbalance through SMOTE and augmentation strategies, and conducted a systematic comparison of deep learning techniques to determine which follow-up stage offers greater diagnostic utility and which architectures perform most effectively at each stage. We benchmarked CNNs, LSTMs, CNN–LSTM hybrids, ResNets, attention-augmented CNNs, Vision Transformers (2D/3D), Swin Transformers, and Mamba-based hybrids across two clinically relevant time points: (1) the first follow-up after radiation therapy and before adjuvant chemotherapy, and (2) the second follow-up after combined chemoradiotherapy. By harmonizing preprocessing protocols and employing patient-level cross-validation, we present the first stage-specific comparative evaluation of modern deep learning models in longitudinal glioma imaging. Our findings establish a rigorous benchmark that not only guides methodological choices for machine learning researchers but also delivers translational insights for neuro-oncology, underscoring the importance of stage-adaptive modeling strategies in clinical decision support.

Table 1. Previous Papers Dataset’s Patients Amount.

Reference	# of Patients	# of TP & PsP	Imaging Type	Method	Performance
Hu et al. (2011)	31	TP=15/PsP=16	T1, T2, FLAIR, TTP, DWI, DSC, MTT	One-class SVM	AUROC= 0.9439 AUC= 0.875
Qian et al. (2016)	35	TP=22/PsP=13	DTI	Math Equation	Accuracy= 77%
Zhang et al. (2016)	79	TP=56/PsP=23	DTI	SVM	AUC= 0.87
Booth et al. (2017)	26	TP=15/PsP=9	T2	SVM	Accuracy= 86%
Ismail et al. (2018)	105	TP=34/PsP=71	T1, T1C	SVM	AUC= 90.2%
Jang et al. (2018)	78	TP=48/PsP=30	T1, T1C	CNN+LSTM	AUC=0.83
Li et al. (2019)	84	TP=61/PsP=23	DT1	DC-AL GAN+SVM	Accuracy= 92%
Kim et al. (2019)	95	TP=49/PsP=46	T1, T1C, FLAIR, DWI, DSC	Generalized linear model	AUC= 0.96 Accuracy=95%
Elshafeey et al. (2019)	105	TP=83/PsP=22	DSE, DSC	SVM	AUC= 0.89 Accuracy=90.82%
Bani-sadr et al. (2019)	76	TP=53/PsP=23	T1, T1C, FLAIR	Random Forest	AUC=0.85 Accuracy= 79.2%
Lee et al. (2020)	23	---	T1, T1C, T2, T2FLAIR, DWI, T1-post-T1-minus. pre-contrast, T2 minus FLAIR	CNN+LSTM	AUC= 0.81

Jang et al. (2020)	104	TP=66/PsP=38	T1C	CNN	AUC= 0.86
Liu et al. (2020)	84	TP=61/PsP=23	DT1	CNN	AUC= 0.98 Accuracy=88% AUC= 0.919
Akbari et al. (2020)	83	TP=63/PsP=20	T1, T1C, T2, T2FLAIR, DTI, DSC	SVM	Accuracy= 87.3%
Lohmann et al. (2020)	34	TP=18/PsP=16	FET-PET	Random Forest	AUC=0.73 Accuracy= 70%
Kebir et al. (2020)	44	TP=30/PsP=14	EFT-PET	Linear Discriminant analysis	AUC= 0.93
Sun et al. (2021)	77	TP=51/PsP=26	T1C	Random Forest	Accuracy=72.78%
Barine et al. (2021)	35	PsP=8/Other=27	T1C	Random Forest	AUC= 0.82
Moassefi et al. (2022)	124	TP=61/PsP=63	T1, T2	3D-DenseNet	AUC=0.756 Accuracy=76.4%
Ari et al. (2022)	131	TP=64/PsP=67	T1C	Generalized Boosted Regression Models	AUC= 0.915 Accuracy= 76.04%
McKenney et al. (2022)	74	TP= 57/PsP=17	T1	Recursive Feature Elimination Random Forest Classifier	AUC= 0.6
Warner et al. (2023)	50	TP= 37/PsP=13	T1, T1C, T2, T2FLAIR	geographically-weighted regression	AUC above 0.6
Yadav et al. (2024)	75	TP= 55/PsP=20	T1, T1C, T2FLAIR	SVM	Accuracy= 85%
Lv et al. (2025)	52	re-lapse=42/PsP=10	T1, T2	CFINet	AUC= 0.929 Accuracy= 95.4%
Gomaa et al. (2025)	79	TP= 45/PsP=34	T1C, T2FLAIR	ViT	AUC= 0.753 Accuracy= 75%
Wang et al. (2025)	114	TP= 69/PsP= 45	T1C	3D-CNN	AUC= 0.74

2. Methods

We systematically developed and benchmarked a diverse set of architectures to interrogate post-treatment glioblastoma MRI, spanning conventional 3D CNNs and ResNets, sequential models (LSTM-based), transformer variants (2D/3D ViT, Swin Transformer), Mamba model and novel hybrids that combine CNNs with attention, LSTM, shift windows patching, or Mamba state-space modules. The detailed architectures of these models are provided in Supplementary Materials.

To systematically investigate how model architecture and clinical stage affect predictive performance, we developed a standardized pipeline encompassing dataset curation, preprocessing, model implementation, training/validation, and evaluation. The workflow was designed to ensure reproducibility, prevent information leakage, and provide a fair basis for comparison across architectures.

2.1. Dataset and preprocessing

We used the Burdenko Glioblastoma Progression Dataset (Burdenko-GBM-Progression), <https://www.cancerimagingarchive.net/collection/burdenko-gbm-progression/>.

comprising 180 patients with primary glioblastoma treated between 2014 and 2020. The dataset includes multi-sequence MRI, CT, clinical, and molecular data; for this study we focused exclusively on contrast-enhanced T1-weighted MRI (T1C), the most widely available and clinically relevant sequence for follow-up assessment. Imaging was acquired on scanners from four vendors with heterogeneous protocols, reflecting real-world clinical variability. The dataset is publicly available through The Cancer Imaging Archive (TCIA).

All T1C volumes were standardized through a multi-stage pipeline (Fig. 1). First, raw DICOM series were converted to NIfTI format and subjected to quality control. Implausible acquisitions were excluded using geometry thresholds on voxel spacing, anisotropy, and slice thickness; among valid candidates, the volume with the highest clarity score was selected per timepoint. Logs and slice previews were generated for auditability. Retained volumes were resampled to 128^3 voxels, skull-stripped, rigidly registered to MNI152 space, and z-score normalized within the brain mask to ensure cross-subject consistency. Deterministic image-label pairing ensured reproducibility at the patient level. For training, data imbalance was mitigated through oversampling and augmentation. Synthetic 3D MR volumes were generated using a lightweight autoencoder with latent-space interpolation, and mild perturbations (small affine transforms, Gaussian noise) were applied to both real and synthetic data. Full implementation details, including thresholds and parameter settings, are provided in the Supplementary Methods.

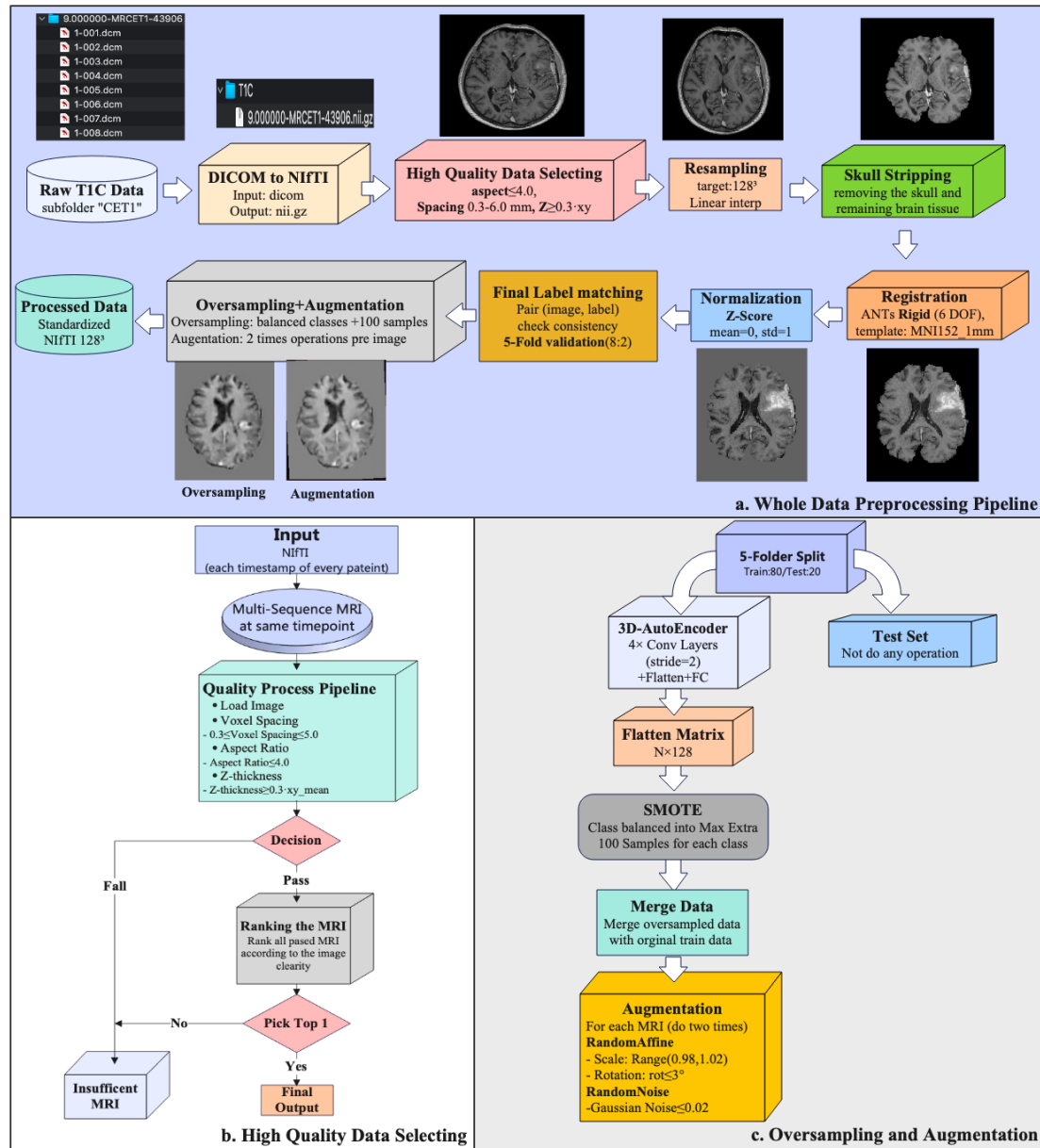


Figure 1. Preprocessing workflow. (a) Whole-set pipeline from raw TIC identification to standardized outputs. (b) High-quality selection logic per patient-timepoint with explicit geometry thresholds and clarity-score ranking; per-series CSV logging and preview generation. (c) Training-only oversampling and augmentation: 3D AE latent-space SMOTE with decoding to 3D volumes augmentations; validation/test splits remain unmodified.

2.2. Labeling strategy

In the Burdenko dataset, each follow-up visit is annotated with a clinical label, which can vary over time. To create a single, reproducible outcome label per patient, we developed a consolidation framework in consultation with a neuro-oncologist. The rules were as follows:

- Progression override: Any evidence of true progression at any timepoint defined the patient as Progression, irrespective of prior or subsequent labels, given its clinical impact.
- Pseudoprogression: A patient was labeled PsP if the most recent follow-up indicated PsP and no prior imaging confirmed progression. PsP was also retained if initial PsP was followed by stability or response without subsequent progression.

- Stable disease: Patients with ≥ 3 consecutive follow-ups showing only stability or response, without new progression, were labeled Stable.
- Scarce follow-up: For patients with ≤ 2 assessments, the most recent report determined the label (PsP if the last scan was PsP, otherwise Progression).
- Distant progression: Cases with new lesions outside the primary site were immediately classified as Progression.

This systematic framework ensured that final labels were clinically meaningful, consistent across patients, and reproducible for downstream modeling.

2.3. Model Architectures

We benchmarked eleven representative DL architectures spanning three design families: 1) Base volumetric models: 3D CNN, LSTM, 3D-ViT, and ResNet. These capture spatial or sequential dependencies directly from T1C volumes. 2) Hybrid models: CNN+LSTM, CNN+SE Attention, and 2D-ViT+LSTM. These combine local convolutional features with sequential or attention-based mechanisms. 3) Advanced models: 3D Swin Transformer, Swin CNN, Vision Mamba, and CNN–Mamba hybrid, which incorporate hierarchical attention or state-space modeling for efficient long-range dependency capture. Architectures were chosen to represent the spectrum of contemporary strategies: convolutional inductive biases, recurrent modeling of slice order, attention-based global context, and state-space efficiency. All models were trained under the same preprocessing, augmentation, and patient-level cross-validation pipeline, ensuring that observed performance differences reflected architecture rather than implementation. Architecture of the base volumetric models and hybrid models are provided in the Supplementary Figures 1 – 7 Methods. The details of developed models for the advanced models are described as follows:

Shift Windows Transformer (Swin Transformer) - To reduce the quadratic cost of global attention, Swin Transformer introduces windowed self-attention with shifted windows and a hierarchical (pyramidal) design, yielding strong accuracy–efficiency trade-offs. For volumetric MRI, the input T1C volume ($1 \times 128 \times 128 \times 128$) was partitioned into non-overlapping $4 \times 4 \times 4$ patches and linearly embedded, as shown in Fig. 2(a). The token grid was processed by four 3D Swin stages (W-MSA/SW-MSA + MLP with residual connections and layer normalization). Channel widths increased $48 \rightarrow 96 \rightarrow 192 \rightarrow 384$ with patch-merging down sampling the resolution $32^3 \rightarrow 16^3 \rightarrow 8^3 \rightarrow 4^3$, enabling cross-window interaction while controlling compute. The final feature map was aggregated by AdaptiveAvgPool3D (1,1,1), projected to 128 dimensions, and passed to a linear–SoftMax classifier ($128 \rightarrow 3$) to yield class probabilities. This formulation captures long-range volumetric dependencies efficiently while preserving locality through windowed attention.

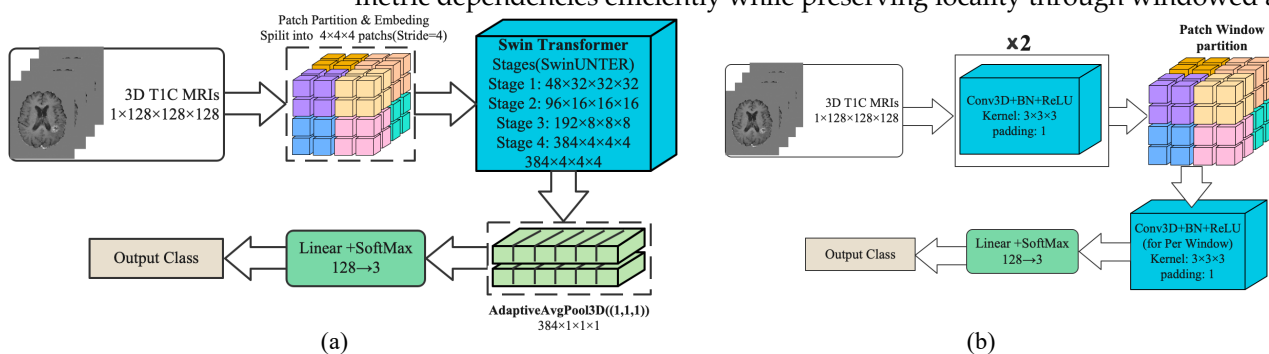


Figure 2. The architecture of the developed Swin based models (a) 3D-Swin Transformer (b) Swin CNN (architectures).

Shift Window Patching CNN (Swin CNN) - Despite recent transformer variants, convolutional networks remain highly efficient for volumetric data because shared $3 \times 3 \times 3$ kernels capture local structure with modest parameters. We therefore adopted a 3D-CNN that borrows the window shift idea from Swin: the input T1C volume ($1 \times 128 \times 128 \times 128$) was first processed by two Conv3D–BatchNorm–ReLU blocks (kernel 3^3 , padding 1) to extract low-level features, which is shown in Fig. 2(b). The resulting feature map was then partitioned into fixed-size 3D windows, within which an additional per-window Conv3D–BN–ReLU was applied. To allow limited cross-window interaction while preserving locality, a second pass with shifted windows (offset by half the window size) can be performed; in practice, this yielded stable performance without materially increasing memory. Window-local convolutions focus capacity on fine anatomical details and constrain computation/memory, while the initial global blocks provide broader context. Features were aggregated (global pooling to a 128-D vector) and fed to a linear–SoftMax head ($128 \rightarrow 3$) to produce class probabilities.

2D Linear-Time Sequence Modeling with Selective State Spaces (2D-Mamba) - Mamba is a selective state-space model (SSM) introduced for long-sequence modeling with linear-time complexity; vision adaptations (often called *Vision Mamba*) map 2D grids to scan orders processed by SSM blocks, offering competitive accuracy with fewer parameters than attention-based transformers. In Fig. 3, each preprocessed T1-contrast (T1C) volume was represented as an ordered set of 50 axial slices. Slices were pad/crop–normalized to 128×128 , then resized to 224×224 and channel-expanded (grayscale replicated) to match ImageNet-style pretraining. A Vision-Mamba tiny backbone produced a 384-dimensional embedding per slice, yielding a sequence of shapes 50×384 . Sequence features were mean-pooled to a volume-level descriptor, projected to 128 dimensions, and passed to a linear–SoftMax classifier to output three class probabilities. By using SSM blocks to capture long-range dependencies within slices while aggregating across slices with lightweight pooling, this model retains global contextual modeling with favorable computational efficiency.

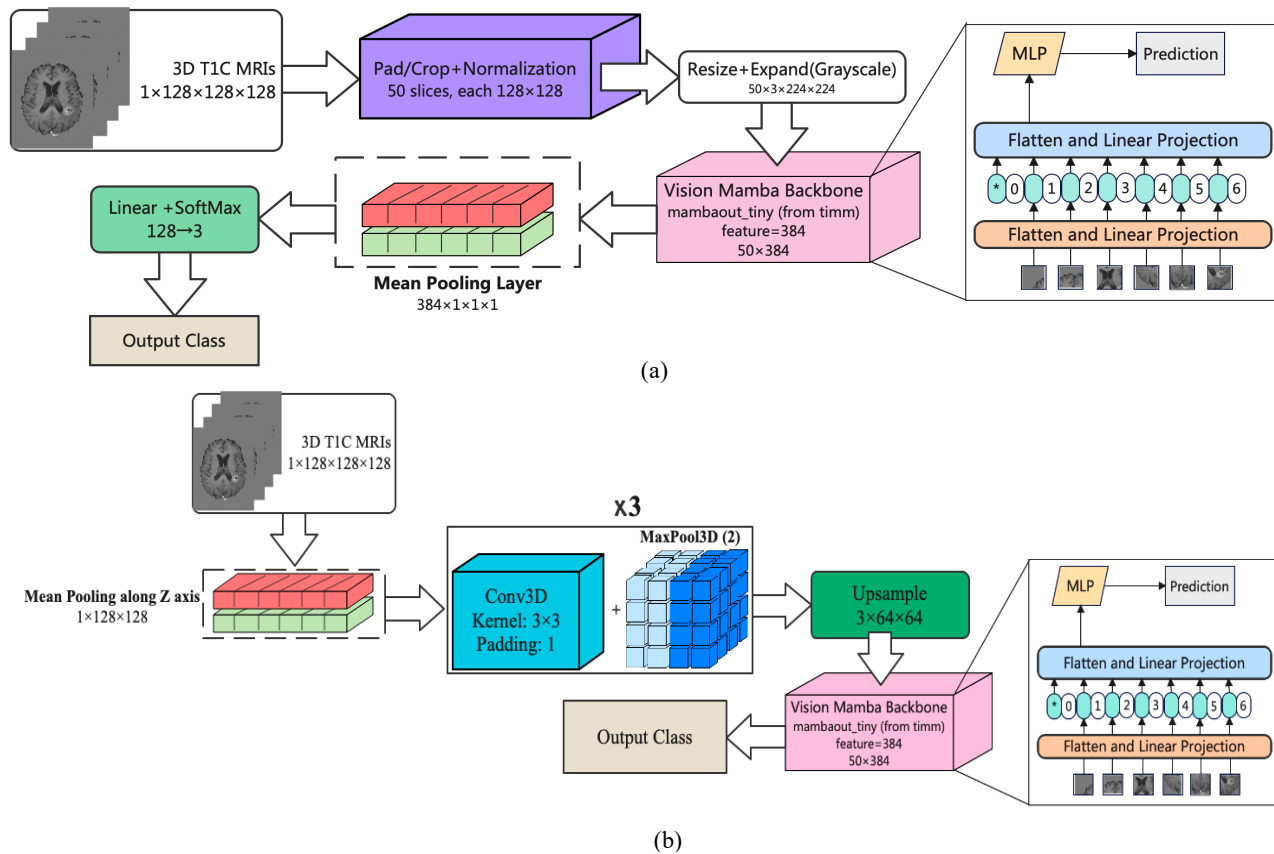


Figure 3. The architecture of the developed Mamba-based models (a) 2D Mamba (b) 2D Mamba+CNN architectures.

2D-Mamba Hybrid with CNN - Mamba is a selective state-space model (SSM) introduced for long-sequence modeling with linear-time complexity; vision adaptations (often called *Vision Mamba*) map 2D grids to scan orders processed by SSM blocks, offering competitive accuracy with fewer parameters than attention-based transformers. In Fig. 3, each preprocessed T1-contrast (T1C) volume was represented as an ordered set of 50 axial slices. Slices were pad/crop-normalized to 128×128 , then resized to 224×224 and channel-expanded (grayscale replicated) to match ImageNet-style pretraining. A Vision-Mamba tiny backbone produced a 384-dimensional embedding per slice, yielding a sequence of shapes 50×384 . Sequence features were mean-pooled to a volume-level descriptor, projected to 128 dimensions, and passed to a linear-SoftMax classifier to output three class probabilities. By using SSM blocks to capture long-range dependencies within slices while aggregating across slices with lightweight pooling, this model retains global contextual modeling with favorable computational efficiency.

3. Results and Discussion

In this section, we present the experimental design and findings of our benchmarking study. We report classification results across first and second follow-ups, followed by analyses of computational efficiency. Together, these results provide a comprehensive assessment of the trade-offs between accuracy, discrimination, and computational cost across model families. Analyses were anchored to two clinically defined follow-ups, evaluated as independent cohorts under identical procedures: (1) the first follow-up after radiotherapy (typically ~ 3 – 4 weeks post-RT), and (2) the second follow-up is after

radiotherapy (typically ~2–3 months post-RT). Treating the stages separately enabled assessment of stage-specific performance.

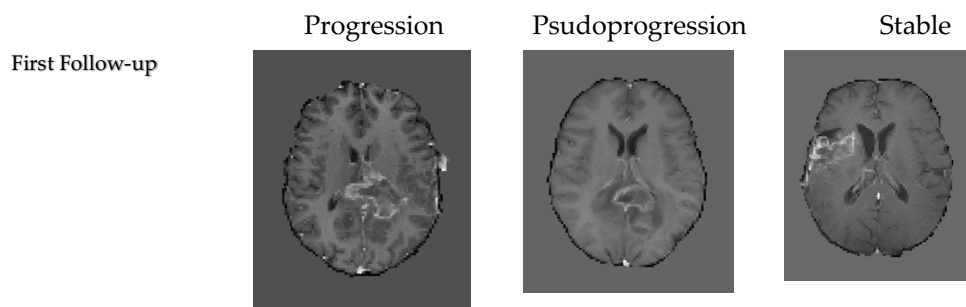
All experiments were implemented in Python (PyTorch/Monai) and executed on a workstation with an NVIDIA RTX A6000 (48 GB) GPU and 128 GB RAM. Unless otherwise noted, models were trained using Adam optimizer (learning rate = $1e-4$), cross-entropy loss, 10 epochs, and random seeds {21, 33, 42}. Batch sizes of 1 and 8 were used for most models, with smaller sizes (1–6) for computationally intensive architectures (Mamba, Swin Transformer). The CNN–Mamba hybrid was further evaluated under batch sizes {1, 2, 4, 8} to assess robustness. Patient-level stratified five-fold cross-validation was used throughout. To prevent information leakage, all preprocessing, augmentation, and synthetic oversampling were fit exclusively on the training split within each fold. Class imbalance was mitigated using latent-space SMOTE applied to autoencoder embeddings, followed by reconstruction into 3D volumes, with caps on synthetic sample counts to avoid over-representation. Mild augmentations (small affine transforms, Gaussian noise) were applied only to training data. We report accuracy, macro-averaged F1 score, and macro-averaged AUC to reflect overall performance and robustness under class imbalance. In addition, we measured computational efficiency: FLOPs, parameter count, average batch inference time, and total training runtime.

Classification performance - Table 2 summarizes predictive performance across both follow-up cohorts. Accuracy values were relatively stable across stages (≈ 0.70 – 0.74), but discrimination improved at the second follow-up, reflected in higher F1 and AUC values for several models. The CNN–Mamba hybrid demonstrated the most consistent trade-off across follow-ups, achieving 74.5% accuracy and F1 = 0.44 at the first follow-up, and improving to 74.1% accuracy and F1 = 0.53 at the second follow-up. This suggests enhanced class separability later in the care pathway. Transformer-based models (3D ViT, 2D ViT+LSTM, Swin Transformer) yielded competitive accuracy and AUC but exhibited higher variance and unstable F1 scores. Lightweight CNNs remained efficient and stable, though their discrimination performance lagged behind. Notably, the highest AUC at the first follow-up was obtained with the 3D ViT (AUC = 0.57, batch = 1), whereas at the second follow-up, the CNN–Mamba hybrid (batch = 4) achieved the strongest AUC (0.66). Representative predictions from the CNN–Mamba hybrid are illustrated in Fig. 13.

Table 2. Summary of Classification Performance (Accuracy, F1-score, and AUC) on First and Second Follow-up MRIs.

Model	First Follow-up			Second Follow-up			
	Accuracy	F1	AUC	Model	Accuracy	F1	AUC
2DViT+LSTM (Batch=1)	0.728 ± 0.0	0.2808 ± 0.0	0.4612 ± 0.0367	2DViT+LSTM (Batch=1)	0.7024 ± 0.0001	0.2749 ± 0.0	0.4869 ± 0.0063
2DViT+LSTM (Batch=8)	0.6885 ± 0.0684	0.2676 ± 0.0228	0.5393 ± 0.028	2DViT+LSTM (Batch=8)	0.7056 ± 0.0055	0.2865 ± 0.0201	0.5319 ± 0.0444
3DViT (Batch=1)	0.7181 ± 0.0154	0.3607 ± 0.0455	0.5728 ± 0.0121	3DViT (Batch=1)	0.724 ± 0.0244	0.4216 ± 0.0412	0.5879 ± 0.0541
3DViT (Batch=8)	0.7257 ± 0.0112	0.3688 ± 0.0452	0.5424 ± 0.0487	3DViT (Batch=8)	0.728 ± 0.0242	0.4162 ± 0.0445	0.6113 ± 0.0425
CNN (Batch=1)	0.6693 ± 0.0216	0.3329 ± 0.0209	0.4655 ± 0.0738	CNN (Batch=1)	0.6324 ± 0.0645	0.3857 ± 0.0778	0.5537 ± 0.0322
CNN (Batch=8)	0.6818 ± 0.0292	0.3304 ± 0.0148	0.4817 ± 0.0378	CNN (Batch=8)	0.6548 ± 0.0351	0.387 ± 0.0556	0.5813 ± 0.0154
CNN+Attention (SE) (Batch=1)	0.7061 ± 0.0213	0.3563 ± 0.0305	0.5439 ± 0.0473	CNN+Attention (SE) (Batch=1)	0.6867 ± 0.0147	0.3878 ± 0.0251	0.5346 ± 0.0453

CNN+Attention (SE) (Batch=8)	0.7011 ± 0.0221	0.3183 ± 0.044	0.5378 ± 0.0299	CNN+Attention (SE) (Batch=8)	0.7061 ± 0.0055	0.3886 ± 0.0065	0.5302 ± 0.0197
CNN+LSTM (Batch=1)	0.728 ± 0.0	0.2808 ± 0.0	0.5257 ± 0.0268	CNN+LSTM (Batch=1)	0.7057 ± 0.0058	0.2903 ± 0.0266	0.5412 ± 0.0199
CNN+LSTM (Batch=8)	0.728 ± 0.0	0.2808 ± 0.0	0.4704 ± 0.0614	CNN+LSTM (Batch=8)	0.7024 ± 0.0	0.2749 ± 0.0	0.4841 ± 0.0632
CNN+ShiftWindowPatch (Batch=1)	0.6341 ± 0.0864	0.3069 ± 0.0738	0.5251 ± 0.0376	CNN+ShiftWindowPatch (Batch=1)	0.6117 ± 0.084	0.2921 ± 0.0257	0.4754 ± 0.0118
CNN+ShiftWindowPatch (Batch=8)	0.728 ± 0.0	0.2808 ± 0.0	0.5 ± 0.0	CNN+ShiftWindowPatch (Batch=8)	0.7024 ± 0.0	0.2749 ± 0.0	0.5 ± 0.0
LSTM (Batch=1)	0.7305 ± 0.0043	0.2989 ± 0.0157	0.5008 ± 0.0723	LSTM (Batch=1)	0.7089 ± 0.0113	0.2649 ± 0.0174	0.4726 ± 0.0134
LSTM (Batch=8)	0.7255 ± 0.0043	0.2803 ± 0.0009	0.5161 ± 0.0511	LSTM (Batch=8)	0.7024 ± 0.0	0.2754 ± 0.0009	0.4638 ± 0.0655
2D-Mamba (16 slices) (Batch=1)	0.7024 ± 0.0	0.2749 ± 0.0	0.5556 ± 0.086	2D-Mamba (16 slices) (Batch=1)	0.6358 ± 0.1154	0.2513 ± 0.0409	0.5336 ± 0.0893
2D-Mamba (16 slices) (Batch=8)	0.7329 ± 0.0084	0.2994 ± 0.0322	0.5604 ± 0.0375	2D-Mamba (16 slices) (Batch=8)	0.7152 ± 0.0148	0.327 ± 0.0625	0.5496 ± 0.039
2D-Mamba (50 slices) (Batch=1)	0.6095 ± 0.1185	0.2413 ± 0.0395	0.5198 ± 0.0539	2D-Mamba (50 slices) (Batch=1)	0.6706 ± 0.055	0.2642 ± 0.0185	0.4687 ± 0.0126
2D-Mamba (50 slices) (Batch=6)	0.735 ± 0.0005	0.3164 ± 0.0162	0.541 ± 0.025	2D-Mamba (50 slices) (Batch=6)	0.7024 ± 0.0	0.2749 ± 0.0	0.5499 ± 0.0481
2D-Mamba+CNN (Batch=1)	0.7451 ± 0.0261	0.4427 ± 0.1143	0.5529 ± 0.0493	2D-Mamba+CNN (Batch=1)	0.7410 ± 0.025	0.5264 ± 0.0565	0.6332 ± 0.0418
2D-Mamba+CNN (Batch=2)	0.716 ± 0.0349	0.3806 ± 0.0229	0.5416 ± 0.0676	2D-Mamba+CNN (Batch=2)	0.7246 ± 0.011	0.4549 ± 0.0092	0.5647 ± 0.0431
2D-Mamba+CNN (Batch=4)	0.7278 ± 0.0297	0.3985 ± 0.0094	0.5464 ± 0.0342	2D-Mamba+CNN (Batch=4)	0.7192 ± 0.011	0.4821 ± 0.0282	0.6617 ± 0.0177
2D-Mamba+CNN (Batch=8)	0.7183 ± 0.0152	0.3795 ± 0.019	0.5622 ± 0.0263	2D-Mamba+CNN (Batch=8)	0.7055 ± 0.0279	0.4022 ± 0.0697	0.6075 ± 0.0233
ResNet (Batch=1)	0.6935 ± 0.0348	0.3331 ± 0.0852	0.4981 ± 0.0519	ResNet (Batch=1)	0.6705 ± 0.0305	0.38 ± 0.0459	0.5744 ± 0.015
ResNet (Batch=8)	0.7157 ± 0.0225	0.3605 ± 0.0401	0.5028 ± 0.0403	ResNet (Batch=8)	0.6708 ± 0.0312	0.4022 ± 0.0426	0.5448 ± 0.0156
Swin Transformer (Batch=1)	0.7009 ± 0.0535	0.2843 ± 0.0198	0.4806 ± 0.039	Swin Transformer (Batch=1)	0.7056 ± 0.011	0.3065 ± 0.0033	0.4921 ± 0.0192
Swin Transformer (Batch=6)	0.3842 ± 0.2114	0.2037 ± 0.0657	0.4789 ± 0.0664	Swin Transformer (Batch=6)	0.4071 ± 0.1748	0.1988 ± 0.062	0.4933 ± 0.0412



Second Follow-up

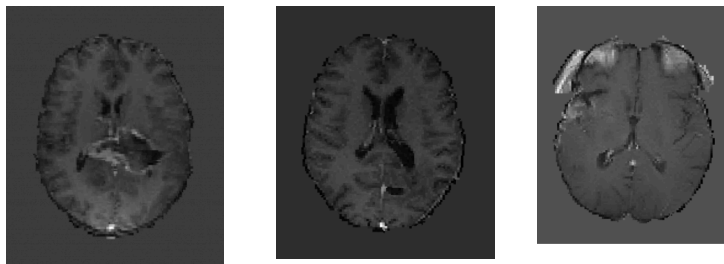


Figure 13. Representative examples of model predictions of the First Follow-up & Second Follow-up’s three classes T1C MRI.

Computational Complexity - We quantify computational efficiency using FLOPs, trainable parameters, average batch inference time, and total training runtime (Table 3). All values are reported as mean ± SD across seeds {21, 33, 42} under the same hardware configuration. Transformer-based models (2D ViT+LSTM, 3D ViT, Swin Transformer) were computationally demanding (≥230 GFLOPs) with runtimes exceeding 1,000 minutes, which challenges clinical deployment despite competitive accuracy/AUC. In contrast, lightweight CNNs were highly efficient (<13 GFLOPs; <0.1M parameters) with stable runtimes, but exhibited lower discrimination.

Table 3. Summary of Computational Complexity and Efficiency Metrics (FLOPs, number of parameters, batch time, and runtime) across Models.

First Follow-up					Second Follow-up				
Model	FLOPs	Params (M)	Batch Time (s)	Run Time (mins)	Model	FLOPs	Params (M)	Batch Time (s)	Run Time (mins)
2DViT+LSTM (Batch=1)	468.6238	5.6421	0.373 ± 0.096	2142.3667 ± 515.5379	2DViT+LSTM (Batch=1)	468.6238	5.6361	0.3045 ± 0.0641	1766.9167 ± 544.7241
2DViT+LSTM (Batch=8)	468.6238	5.6421	3.364 ± 3.9684	2366.75 ± 1640.4337	2DViT+LSTM (Batch=8)	468.6238	5.6361	2.5917 ± 2.7938	1905.4367 ± 1339.13
3DViT (Batch=1)	277.2708	88.166	0.1753 ± 0.107	887.0333 ± 300.3485	3DViT (Batch=1)	277.2708	88.166	0.1922 ± 0.0301	1170.7833 ± 343.5418
3DViT (Batch=8)	277.2708	88.166	1.1301 ± 0.1592	948.2333 ± 143.8502	3DViT (Batch=8)	277.2708	88.166	1.0392 ± 0.2969	1005.91 ± 206.0372
CNN (Batch=1)	12.3889	0.0832	0.044 ± 0.0107	529.7833 ± 80.0649	CNN (Batch=1)	12.3889	0.0832	0.021 ± 0.0169	468.1633 ± 72.6496
CNN (Batch=8)	12.3889	0.0832	0.1439 ± 0.0943	407.6067 ± 100.5402	CNN (Batch=8)	12.3889	0.0832	0.1304 ± 0.0934	390.8433 ± 51.1764
CNN+Attention (SE) (Batch=1)	44.821	2.4304	0.0662 ± 0.0332	596.93 ± 64.7776	CNN+Attention (SE) (Batch=1)	44.821	2.4304	0.0382 ± 0.0141	454.77 ± 32.3068
CNN+Attention (SE) (Batch=8)	44.821	2.4304	0.1636 ± 0.0517	503.3133 ± 178.9891	CNN+Attention (SE) (Batch=8)	44.821	2.4304	3.0258 ± 2.4875	1181.1167 ± 625.8477
CNN+LSTM (Batch=1)	5.6613	1.5707	0.0221 ± 0.0133	549.25 ± 7.9764	CNN+LSTM (Batch=1)	5.6613	1.2707	0.0192 ± 0.0125	430.42 ± 48.5683
CNN+LSTM (Batch=8)	5.6613	1.5707	0.1295 ± 0.0511	490.8967 ± 35.8705	CNN+LSTM (Batch=8)	5.6613	1.2707	0.0801 ± 0.0161	339.8367 ± 76.1156
CNN+Shift-WindowPatch (Batch=1)	0.0255	0.0701	0.0015 ± 0.0007	1114.4133 ± 187.3267	CNN+Shift-WindowPatch (Batch=1)	0.0255	0.0701	0.0022 ± 0.0009	1024.7733 ± 167.7931
CNN+Shift-WindowPatch (Batch=8)	0.0255	0.0701	0.004 ± 0.0036	254.0 ± 114.0537	CNN+Shift-WindowPatch (Batch=8)	0.0255	0.0701	0.0023 ± 0.0007	233.3367 ± 101.256

LSTM (Batch=1)	7.4189	20.381	0.0039 ± 1 0.0013	483.2667 ± 47.298	LSTM (Batch=1)	7.4189	20.381	0.0033 ± 1 0.0019	411.6133 ± 60.9606
LSTM (Batch=8)	7.4189	20.381	0.0253 ± 1 0.0294	416.0533 ± 93.5496	LSTM (Batch=8)	7.4189	20.381	0.0237 ± 1 0.0323	352.1033 ± 81.3641
2D-Mamba (16 slices) (Batch=1)	142.9558	24.515	0.0808 ± 1 0.009	952.81 ± 248.1051	2D-Mamba (16 slices) (Batch=1)	142.9558	24.515	0.1279 ± 1 0.0879	1285.73 ± 666.0025
2D-Mamba (16 slices) (Batch=8)	142.9558	24.515	0.197 ± 1 0.026	471.3967 ± 77.5497	2D-Mamba (16 slices) (Batch=8)	142.9558	24.515	0.1917 ± 1 0.0189	416.2267 ± 56.6206
2D-Mamba (50 slices) (Batch=1)	446.7358	24.515	0.1544 ± 1 0.1406	2567.8533 ± 242.1994	2D-Mamba (50 slices) (Batch=1)	446.7358	24.373	0.0846 ± 4 0.0123	671.695 ± 30.1581
2D-Mamba (50 slices) (Batch=6)	446.7358	24.515	0.2909 ± 1 0.0029	802.0667 ± 13.4718	2D-Mamba (50 slices) (Batch=6)	446.7358	24.420	0.2548 ± 6 0.0518	770.5533 ± 99.2479
2D-Mamba+CNN (Batch=1)	0.7776	24.231	0.0801 ± 6 0.0864	787.97 ± 473.7224	2D-Mamba+CNN (Batch=1)	0.7776	24.231	0.0317 ± 6 0.0169	395.4667 ± 68.7862
2D-Mamba+CNN (Batch=2)	0.7776	24.231	0.0349 ± 6 0.0076	631.7 ± 446.109	2D-Mamba+CNN (Batch=2)	0.7776	24.231	0.015 ± 6 0.003	326.1533 ± 88.3388
2D-Mamba+CNN (Batch=4)	0.7776	24.231	0.0789 ± 6 0.0777	419.1267 ± 92.8542	2D-Mamba+CNN (Batch=4)	0.7776	24.231	0.1213 ± 6 0.1818	427.9933 ± 153.0907
2D-Mamba+CNN (Batch=8)	0.7776	24.231	0.1595 ± 6 0.238	372.4667 ± 109.4993	2D-Mamba+CNN (Batch=8)	0.7776	24.231	0.1536 ± 6 0.2308	330.58 ± 90.0112
ResNet (Batch=1)	28.4955	0.6528	0.0784 ± 0.1079	511.38 ± 44.35	ResNet (Batch=1)	28.4955	0.7428	0.0169 ± 0.0027	416.0133 ± 43.1828
ResNet (Batch=8)	28.4955	0.6528	0.1052 ± 0.0244	331.75 ± 21.3322	ResNet (Batch=8)	28.4955	0.7428	0.1382 ± 0.0465	896.3633 ± 829.5617
Swin Transformer (Batch=1)	236.9559	7.8644	0.7694 ± 0.1436	1324.7833 ± 194.3059	Swin Transformer (Batch=1)	236.9559	7.8644	0.9166 ± 0.3571	1404.7267 ± 300.9926
Swin Transformer (Batch=6)	236.9559	7.8644	0.6069 ± 0.0018	302.81 ± 8.3104	Swin Transformer (Batch=6)	236.9559	7.8644	8.1024 ± 12.9558	265.25 ± 9.3466

The CNN–Mamba hybrid provided the most favorable efficiency–performance balance: a moderate parameter count (~24M) coupled with very low compute (<1 GFLOP) and reasonable runtime, while maintaining the most consistent Accuracy–F1 trade-off across both follow-ups. These characteristics suggest a more practical path toward resource-constrained clinical environments than transformer variants, without the performance drops observed for ultra-light CNNs.

To conclude, the empirical evidence demonstrates that the hybrids of convolutional and Linear-Time Sequence Modeling with Selective State Spaces (Mamba+CNN) consistently yield the best trade-off between predictive cost and computational cost. At both follow-up MRIs, Mamba+CNN had the most stable performance with accuracy and a significantly improved F1-score in the second follow-up, indicating that it could capture spatial and temporal dependencies. While Transformer-based models showed strong accuracy and AUC, their computational requirements prohibited their use in real clinical settings. On the other hand, efficient CNNs were computationally inexpensive, but the quality of classification dropped significantly. Although Mamba+CNN achieved the best performance across most metrics and performed best with smaller batch sizes, it did not obtain the highest AUC. At the first follow-up, the highest AUC was achieved by the 3D-ViT with a batch size of 1, while at the second follow-up, the CNN+Mamba with a batch size

of 4 achieved the highest AUC. The Mamba+CNN model's predicted results for each class are shown in Fig. 13.

Limitation – We analyzed the first and second follow-up scans as independent cohorts to isolate stage effects, but did not model longitudinal trajectories or impute missing visits, approaches that could capture disease dynamics. The dataset is still relatively small (n=180) and imbalanced; despite multi-seed patient-level cross-validation, external multi-center validation remains necessary. The CNN–Mamba hybrid did not dominate every metric (e.g., 3D-ViT had the top AUC at the first follow-up), and we restricted inputs to T1C MRI; adding multi-sequence MRI and clinical/molecular covariates may improve especially macro-F1.

4. Conclusion

We presented the first stage-specific benchmarking of deep learning architectures for differentiating true progression from pseudoprogression in glioblastoma using follow-up MRI. Evaluating eleven model families within a unified, quality-controlled pipeline, we found that overall performance remains moderate but improves at later follow-ups, consistent with richer clinical separability between treatment effects and true recurrence over time. These results establish a stage-aware benchmark for follow-up MRI analysis in glioblastoma and underscore the importance of standardized, leakage-aware training and evaluation protocols for this challenging task.

At the architectural level, our findings extend prior work on hybrid models for medical imaging by systematically comparing CNNs, transformers, and state-space-based approaches in longitudinal glioblastoma follow-ups. A CNN–Mamba hybrid provided the most reliable trade-off between predictive accuracy and computational efficiency, whereas transformer-based models (e.g., ViT, Swin) achieved competitive accuracy and AUC at the cost of higher computational burden and more variable F1 scores. In contrast, lightweight CNNs were highly efficient in terms of FLOPs and parameter counts but exhibited lower discrimination, reflecting the difficulty of handling class imbalance and complex spatiotemporal patterns in this setting. Broader validation on multi-center, multi-sequence cohorts, incorporation of clinical and molecular covariates, and exploration of self-supervised and model-compression strategies will be critical next steps toward practical deployment of automated follow-up MRI analysis in neuro-oncology.

Author Contributions: methodology, formal analysis, original draft preparation W G, Gm did the supervision, review and editing.

Funding: This research has no funding.

Acknowledgments: The authors thank Dr. Pierre Giglio, MD, Director of Neuro-Oncology at The Ohio State University Wexner Medical Center, for his advice on MRI labeling and for reviewing the labeling strategy.

Conflicts of Interest: The authors declare no conflict of interest.

Reference

1. Ahsan, M. M., Raman, S., Liu, Y., & Siddique, Z. (2025). Hybrid oversampling technique for imbalanced pattern recognition: Enhancing performance with Borderline Synthetic Minority oversampling and Generative Adversarial Networks. *Machine Learning with Applications*, 13, 100637. <https://doi.org/10.1016/j.mlwa.2025.100637>
2. Blakstad, E., Solheim, K. M., Rygh, A. M., Andreassen, O. A., Torp, T., & Helland, K. B. (2023). Diagnostic challenges of pseudoprogression in glioblastoma: A review of current literature. *Cancers*, 15(5), 1492. <https://doi.org/10.3390/cancers15051492>

3. Demircioğlu, A. (2024). Applying oversampling before cross-validation will lead to high bias in radiomics. *Scientific Reports*, *14*, 11563. <https://doi.org/10.1038/s41598-024-62585-z>
4. Gomaa, A., Huang, Y., Stephan, P., Breining, K., Frey, B., Dörfler, A., Schnell, O., Delev, D., Coras, R., Schmitter, C., Stritzelberger, J., Semrau, S., Maier, A., Bayer, S., Schönecker, S., Heiland, D. H., Hau, P., Gaip, U. S., Bert, C., ... Putz, F. (2024). A self-supervised multimodal deep learning approach to differentiate post-radiotherapy progression from pseudoprogression in glioblastoma. *arXiv preprint arXiv:2502.03999*. <https://doi.org/10.48550/arXiv.2502.03999>
5. Gong, Y., Wu, Q., Zhou, M., & Chen, C. (2025). A diversity and reliability-enhanced synthetic minority over-sampling technique for multi-label learning. *Information Sciences*, *690*, 121579. <https://doi.org/10.1016/j.ins.2024.121579>
6. Hu, X., Wong, K. K., Young, G. S., Guo, L., & Wong, S. T. (2011). Support vector machine multiparametric MRI identification of pseudoprogression from tumor recurrence in patients with resected glioblastoma. *Journal of Magnetic Resonance Imaging*, *33*(2), 296–305. <https://doi.org/10.1002/jmri.22432>
7. Jang, B.-S., Jeon, S. H., Kim, I. H., & Kim, I. A. (2018). Prediction of pseudoprogression versus progression using machine learning algorithm in glioblastoma. *Scientific Reports*, *8*, 12516. <https://doi.org/10.1038/s41598-018-31007-2>
8. Kalata, I. K., Khan, R., & Nakarmi, U. (2024). Learning from oversampling: A systematic exploitation of over-sampling to address data scarcity issues in deep learning-based magnetic resonance image reconstruction. *IEEE Access*, *12*, 10591992. <https://doi.org/10.1109/ACCESS.2024.3426362>
9. Lee, J., Wang, N., Turk, S., Mohammed, S., Lobo, R., Kim, J., Liao, E., Camelo-Piragua, S., Kim, M., Junck, L., Bapuraj, J., Srinivasan, A., & Rao, A. (2020). Discriminating pseudoprogression and true progression in diffuse infiltrating glioma using multi-parametric MRI data through deep learning. *Scientific Reports*, *10*, 20331. <https://doi.org/10.1038/s41598-020-77389-0>
10. Li, M., Ren, X., Dong, G., Wang, J., Jiang, H., Yang, C., Zhao, X., Zhu, Q., Cui, Y., Yu, K., & Lin, S. (2021). Distinguishing pseudoprogression from true early progression in isocitrate dehydrogenase wild-type glioblastoma by interrogating clinical, radiological, and molecular features. *Frontiers in Oncology*, *11*, 627325. <https://doi.org/10.3389/fonc.2021.627325>
11. Li, M., Tang, H., Chan, M. D., Zhou, X., & Qian, X. (2019). DC-AL GAN: Pseudoprogression and true tumor progression of glioblastoma multiforme image classification based on DCGAN and AlexNet. *arXiv preprint arXiv:1902.06085*. <https://doi.org/10.48550/arXiv.1902.06085>
12. Liu, R., Hall, L. O., Bowyer, K. W., Goldgof, D. B., Gatenby, R., & Ben Ahmed, K. (2017). Synthetic minority image over-sampling technique: How to improve AUC for glioblastoma patient survival prediction. In *Proceedings of the IEEE Systems, Man, and Cybernetics Conference* (pp. 1357–1362). <https://doi.org/10.1109/SMC.2017.8122802>
13. Lv, Y., Liu, J., Tian, X., Yang, P., & Pan, Y. (2025). CFINet: Cross-modality MRI feature interaction network for pseudoprogression prediction of glioblastoma. *Journal of Computational Biology*, *32*(2), 212–224. <https://doi.org/10.1089/cmb.2024.0518>
14. McKenney, A. S., Weg, E., Bale, T. A., Wild, A. T., Um, H., Fox, M. J., Lin, A., Yang, J. T., Yao, P., Birger, M. L., Tixier, F., Sellitti, M., Moss, N. S., Young, R. J., & Veeraraghavan, H. (2022). Radiomic analysis to predict histopathologically confirmed pseudoprogression in glioblastoma patients. *Advances in Radiation Oncology*, *8*(1), 100916. <https://doi.org/10.1016/j.adro.2022.100916>
15. Moassefi, M., Faghani, S., Conte, G. M., Kowalchuk, R. O., Vahdati, S., Crompton, D. J., Perez-Vega, C., Domingo Cabreja, R. A., Vora, S. A., Quiñones-Hinojosa, A., Parney, I. F., Trifiletti, D. M., & Erickson, B. J. (2022). A deep learning model for discriminating true progression from pseudoprogression in glioblastoma patients. *Journal of Neuro-Oncology*. <https://doi.org/10.1007/s11060-022-04080-x>

16. Sim, Y., Kim, M., Kim, J., Lee, S.-K., Han, K., & Sohn, B. (2024). Multiparametric MRI-based radiomics model for predicting human papillomavirus status in oropharyngeal squamous cell carcinoma: Optimization using oversampling and machine learning techniques. *European Radiology*, *34*, 3102–3112. <https://doi.org/10.1007/s00330-023-10338-3>
17. Sun, Y.-Z., Yan, L.-F., Han, Y., Nan, H.-Y., Xiao, G., Tian, Q., Pu, W.-H., Li, Z.-Y., Wei, X.-C., Wang, W., & Cui, G.-B. (2021). Differentiation of pseudoprogression from true progression in glioblastoma patients after standard treatment: A machine learning strategy combined with radiomics features from T1-weighted contrast-enhanced imaging. *BMC Medical Imaging*, *21*(1), 17. <https://doi.org/10.1186/s12880-020-00545-5>
18. Taal, W. A., Brandsma, P. C., de Bruin, J. F. M., Bromberg, M. C., van Es, M., Hovinga, M. J., & van den Bent, M. J. (2008). Incidence of early pseudo-progression in a cohort of malignant glioma patients treated with chemoradiation with temozolomide. *Cancer*, *113*(2), 405–410. <https://doi.org/10.1002/cncr.23562>
19. Taylor, L. P., Nwagwu, M. M., Marquez, C. C., et al. (2022). Pseudoprogression versus true progression in glioblastoma: What neurosurgeons need to know. *Scientific Reports*, *12*, 13012. <https://doi.org/10.1038/s41598-022-16726-x>
20. Turk, S., Wang, N. C., Kitis, O., Mohammed, S., Ma, T., Lobo, R., Kim, J., Camelo-Piragua, S., Johnson, T. D., Kim, M. M., Junck, L., Moritani, T., Srinivasan, A., Rao, A., & Bapuraj, J. R. (2022). Comparative study of radiologists vs. machine learning in differentiating biopsy-proven pseudoprogression and true progression in diffuse gliomas. *Neuroscience Informatics*, *2*(3), 100088. <https://doi.org/10.1016/j.neuri.2022.100088>
21. Wang, J., & Awang, N. (2025). A novel synthetic minority oversampling technique for multiclass imbalance problems. *IEEE Access*, *13*, 10829925. <https://doi.org/10.1109/ACCESS.2025.3326246>
22. Warner, E., Lee, J., Krishnan, S., Wang, N., Mohammed, S., Srinivasan, A., Bapuraj, J., & Rao, A. (2023). Low-parameter supervised learning models can discriminate pseudoprogression and true progression in non-perfusion-based MRI. In *Proceedings of the IEEE Engineering in Medicine and Biology Conference* (pp. 1–4). <https://doi.org/10.1109/EMBC40787.2023.10340435>
23. Yadav, A. P., Akkurt, B. H., Musigmann, M., Mammadov, O., Blömer, D. A., Kasap, D. N. G., Henssen, D. J. H. A., Nacul, N. G., Sartoretti, E., Sartoretti, T., Backhaus, P., Thomas, C., Stummer, W., Heindel, W., & Mannil, M. (2022). Pseudoprogression prediction in high grade primary CNS tumors by use of radiomics. *Scientific Reports*, *12*, 5915. <https://doi.org/10.1038/s41598-022-09945-9>
24. Yadav, V. K., Mohan, S., Agarwal, S., de Godoy, L. L., Rajan, A., Nasrallah, M. P., Bagley, S. J., Brem, S., Loevner, L. A., & Poptani, H. (2024). Distinction of pseudoprogression from true progression in glioblastomas using machine learning based on multiparametric magnetic resonance imaging and O6-methylguanine-methyltransferase promoter methylation status. *Neuro-Oncology Advances*, *6*(1), vdae159. <https://doi.org/10.1093/ona-jnl/vdae159>
25. Zhang, X., & Noshadravan, A. (2025). Efficient reliability analysis for offshore wind turbines: Leveraging SVM and augmented oversampling technique. *Structural Safety*, *115*, 102597. <https://doi.org/10.1016/j.strusafe.2025.102597>
26. Zolotova, S. V., Golanov, A. V., Pronin, I. N., Dalechina, A. V., Nikolaeva, A. A., Belyashova, A. S., Usachev, D. Y., Kondrateva, E. A., Druzhinina, P. V., Shirokikh, B. N., Saporov, T. N., Belyaev, M. G., & Kurmukov, A. I. (2023). *Burdenko's Glioblastoma Progression Dataset (Burdenko-GBM-Progression)* (Version 1) [Data set]. The Cancer Imaging Archive. <https://doi.org/10.7937/E1QP-D183>
27. Bhandari, A., Marwah, R., Smith, J., Nguyen, D., Bhatti, A., Lim, C. P., & Lasocki, A. (2022). Machine learning imaging applications in the differentiation of true tumour progression from treatment-related effects in brain tumours: A systematic review and meta-analysis. *Journal of Medical Imaging and Radiation Oncology*, *66*(6), 781–797. <https://doi.org/10.1111/1754-9485.13436>
28. Jang B-S, Park AJ, Jeon SH et al. Machine learning model to predict pseudoprogression versus progression in glioblastoma using MRI: a multi-institutional study (KROG 18-07). *Cancer* 2020; *12*: 2706.

29. Ismail M, Hill V, Statsevych V et al. Shape features of the lesion habitat to differentiate brain tumor progression from pseudoprogression on routine multiparametric MRI: a multisite study. *AJNR Am J Neuroradiol* 2018; 39: 2187–93.
30. Zhang J, Yu H, Qian X et al. Pseudo progression identification of glioblastoma with dictionary learning. *Comput Biol Med* 2016; 73: 94–101.
31. Qian X, Tan H, Zhang J et al. Stratification of pseudoprogression and true progression of glioblastoma multiform based on longitudinal diffusion tensor imaging without segmentation. *Med Phys* 2016; 43: 5889.
32. Kebir S, Schmidt T, Weber M et al. A preliminary study on machine learning-based evaluation of static and dynamic FET-PET for the detection of pseudoprogression in patients with IDH-wildtype glioblastoma. *Cancers (Basel)* 2020; 12: 3080.
33. Lohmann P, Elahmadawy MA, Gutsche R et al. FET PET radiomics for differentiating pseudoprogression from early tumor progression in glioma patients postchemoradiation. *Cancer* 2020; 12: 3835.
34. Liu X, Zhou X, Qian X. Transparency-guided ensemble convolutional neural network for the stratification between pseudoprogression and true progression of glioblastoma multiform in MRI. *J Visual Commun Image Represent* 2020; 72. doi: 10.1016/j.jvcir.2020.102880
35. Akbari H, Rathore S, Bakas S et al. Histopathologyvalidated machine learning radiographic biomarker for non-invasive discrimination between true progression and pseudo-progression in glioblastoma. *Cancer* 2020; 126: 2625–36.
36. Bani-Sadr A, Eker OF, Berner LP et al. Conventional MRI radiomics in patients with suspected early- or pseudoprogression. *Neurooncol Adv* 2019; 1: vdz019.
37. Booth TC, Larkin TJ, Yuan Y et al. Analysis of heterogeneity in T2-weighted MR images can differentiate pseudoprogression from progression in glioblastoma. *PLoS One* 2017; 12: e0176528.
38. Elshafeey N, Kotrotsou A, Hassan A et al. Multicenter study demonstrates radiomic features derived from magnetic resonance perfusion images identify pseudoprogression in glioblastoma. *Nat Commun* 2019; 10: 3170.
39. Kim J, Park JE, Jo Y et al. Incorporating diffusion- and perfusion-weighted MRI into a radiomics model improves diagnostic performance for pseudoprogression in glioblastoma patients. *Neuro Oncol* 2019; 21: 404–14.

Supplementary Document

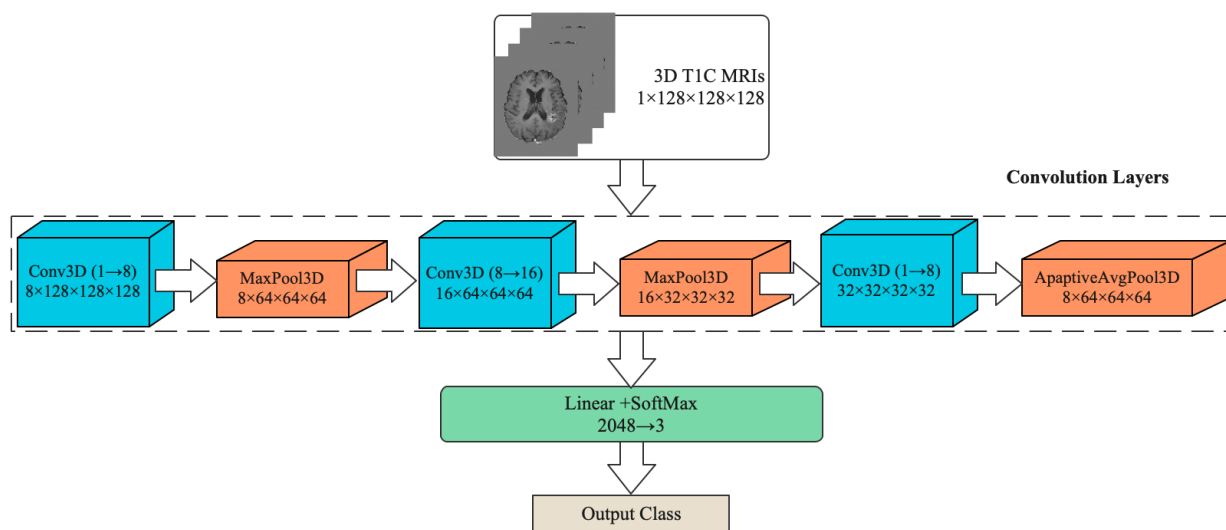


Figure 1. CNN architecture. A compact 3D-CNN was employed to classify preprocessed T1-contrast (T1C) MRI volumes (input $1 \times 128 \times 128 \times 128$). Sequential Conv3D–BatchNorm–ReLU blocks with increasing channels (8→16→32) made up the network. Translation-equivariant volumetric features were produced by convolutions using $3 \times 3 \times 3$ kernels (stride 1, padded). MaxPool3D ($2 \times 2 \times 2$) improved efficiency and resilience to minor misalignments by expanding the receptive field and decreasing spatial resolution after the first two blocks. To produce three class probabilities, features were combined, flattened to a 2048-D vector, and then sent to a linear-softmax head. Through weight sharing and pooling, this design strikes a balance between maintaining the anatomical context and optimizing parameters.

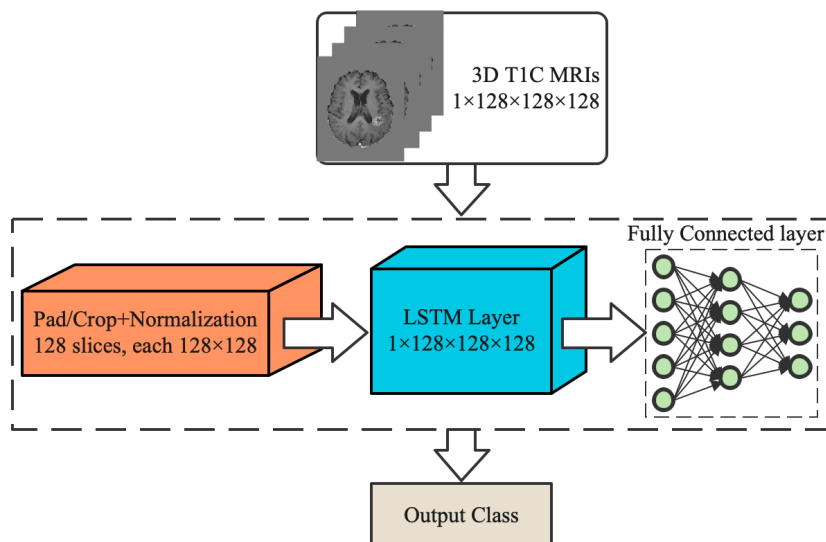


Figure 2. LSTM architecture. Each TIC volume was treated as an ordered sequence of 128 axial slices. The slices were padded/cropped and z-score normalized to 128×128 . At time step t , the vectorized slice (or its low-level features) was fed to a unidirectional LSTM, which used its gating mechanism to decide what new information to store, what past information to discard, and what to expose to the next step. The sequence representation (final hidden state) was passed to a fully connected layer with SoftMax to produce class probabilities. This formulation preserves superior–inferior anatomical continuity while remaining parameter-efficient compared with full 3D convolutions.

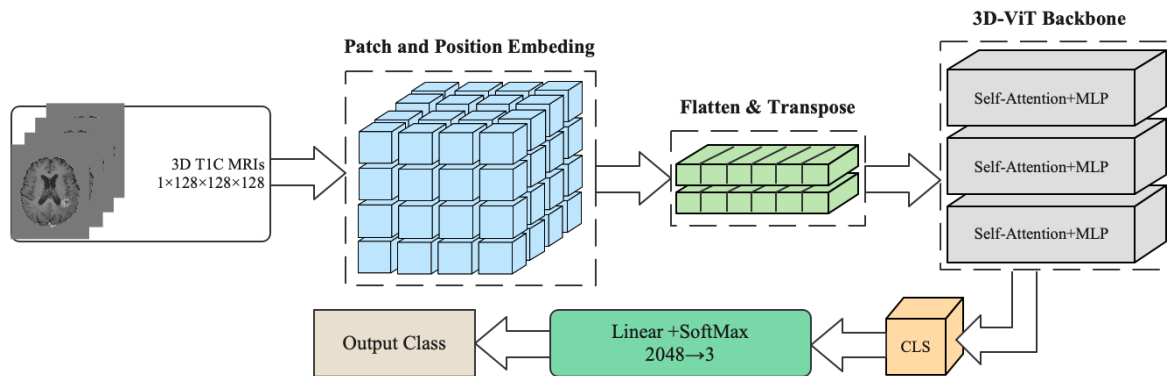


Figure 3. 3D-ViT architecture. Each preprocessed TIC volume ($1 \times 128 \times 128 \times 128$) was partitioned into non-overlapping 3D patches. Each patch was linearly projected to an embedding and augmented with a learnable positional embedding; a class (CLS) token was prepended. The resulting token sequence (after flattening/transposition) was processed by a stack of Transformer encoder blocks (multi-head self-attention + MLP with residual connections and layer normalization), allowing global, cross-patch interactions. The final CLS embedding was passed to a linear–SoftMax head ($2048 \rightarrow 3$) to produce class probabilities. By operating on tokens rather than pixels/voxels, 3D-ViT captured long-range volumetric dependencies while remaining architecture-agnostic to spatial size.

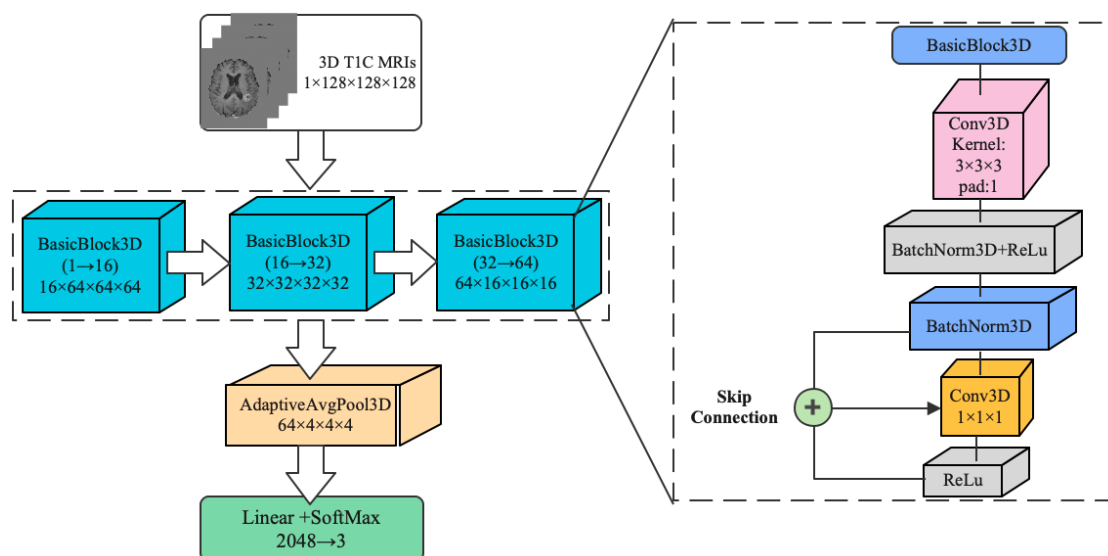


Fig. 4. 3D-ResNet architecture. A volumetric 3D-ResNet is developed, which each BasicBlock3D contains Conv3D→BatchNorm→ReLU→Conv3D→BatchNorm, plus an identity skip; when channel or resolution changes, the skip uses a $1 \times 1 \times 1$ projection with stride to align dimensions. The backbone comprised three stages with increasing channels (8→16, 16→32, 32→64); the first block of each stage downsampled spatially (stride 2), yielding feature maps of roughly $64^3 \rightarrow 32^3 \rightarrow 16^3$. Features were aggregated by AdaptiveAvgPool3D to a fixed grid and flattened to a 2048-dimensional vector, then passed to a linear–SoftMax head to produce three class probabilities. This residual design preserves volumetric context with modest parameter growth and mitigates vanishing-gradient effects compared with plain 3D CNNs.

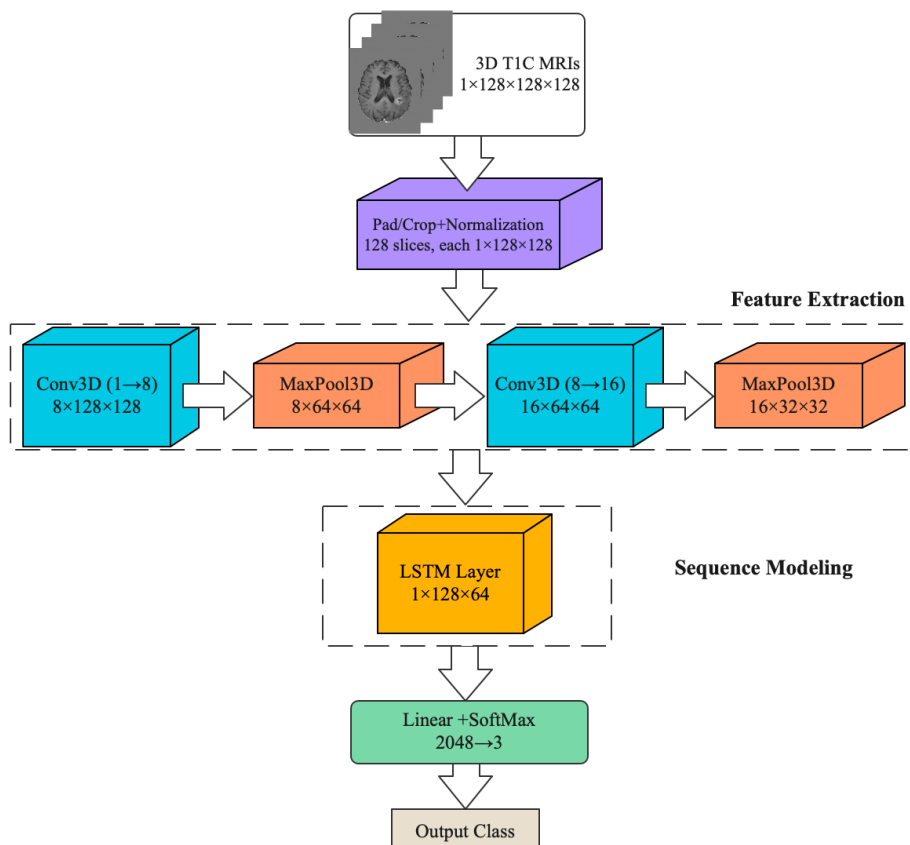


Fig. 5. CNN+LSTM architecture. Convolutional encoders excel at extracting local spatial patterns, whereas recurrent networks, LSTM units—model ordered dependencies. For volumetric MRI, treating the axial stack as a sequence allows us to couple **slice-level feature extraction** with **slice-to-slice context modeling**. As Fig. 5 shows, each preprocessed TIC volume ($1 \times 128 \times 128 \times 128$) was first padded/cropped and z-score normalized per slice. A shallow 3D CNN encoder (Conv3D–BatchNorm–ReLU blocks with interleaved MaxPool3D that downsampled in-plane while preserving depth) produced feature maps that were spatially aggregated over x – y to yield a sequence of 128 slice embeddings. This sequence was passed to a single LSTM layer, whose input, forget, and output gates regulated what new information to store, what past information to discard, and what to expose at each step; the final hidden representation was fed to a fully connected SoftMax classifier to output class probabilities. his CNN+LSTM design, inspired by prior work (e.g., Jang et al., 2018), captures fine-grained local cues within slices and long-range superior–inferior dependencies across the stack, while remaining more parameter-efficient than deep 3D-only models.

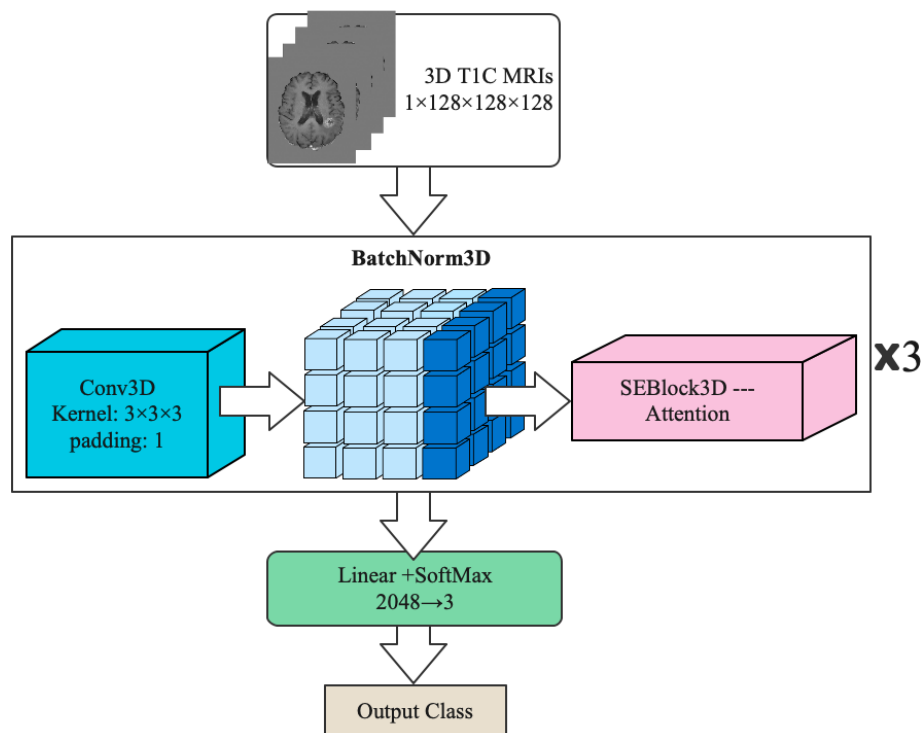


Fig. 6. CNN+SE Attention architecture. Channel-attention improves convolutional features by letting the network emphasize informative channels and suppress distractors. Fig. 6 adopted a volumetric Squeeze-and-Excitation (SE) variant for TIC MRI: the model stacks three identical units, each consisting of a Conv3D layer ($3 \times 3 \times 3$, padding = 1) followed by BatchNorm3D and a 3D-SE block. The SE block first squeezes global spatial information via 3D global average pooling to form a channel descriptor, then excites channels through a small bottleneck (two fully connected layers with nonlinearity and a sigmoid gate) that re-weights the feature maps. After three such units, features are aggregated and flattened to 2048 dimensions, then passed to a linear–softmax head to produce three class probabilities. This architecture preserves local volumetric cues via convolutions while adaptively highlighting lesion-relevant channels through SE attention.

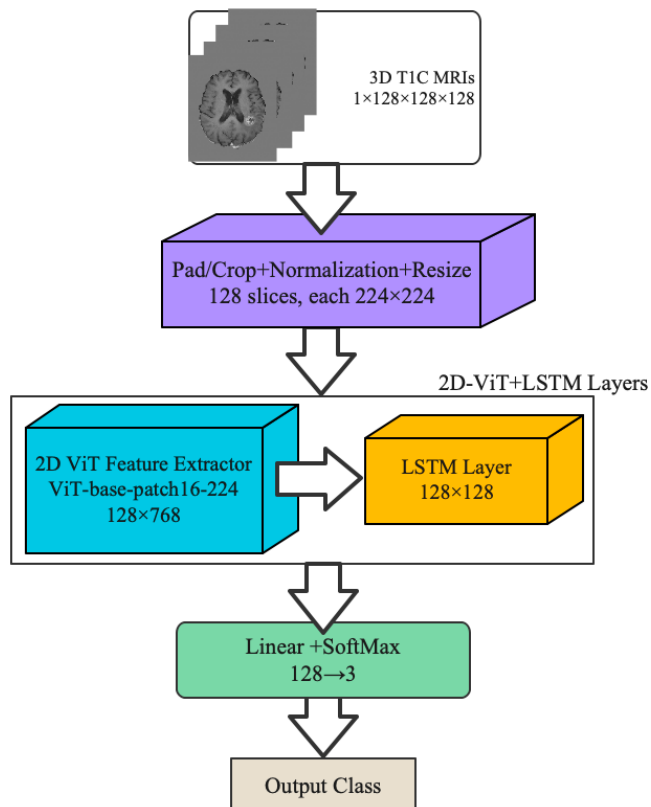


Fig. 7. 2D ViT+LSTM. Transformers capture long-range dependencies by attending over patch tokens; a 2D Vision Transformer (ViT) applies this to single images, whereas volumes also require modeling relationships **across slices**. Fig. 7 shows that each preprocessed TIC volume ($1 \times 128 \times 128 \times 128$) was treated as an ordered stack of **128 axial slices**. Slices were pad/crop-normalized and resized to 224×224 . A **pretrained ViT-Base/16** model served as a per-slice feature extractor, yielding a **768-dimensional** embedding (CLS token) for each slice. The resulting sequence (128×768) was fed to a unidirectional **LSTM** (hidden size = 128); the final hidden state was passed to a linear-SoftMax layer ($128 \rightarrow 3$) to produce class probabilities. This design leverages ViT for **global within-slice** context and LSTM for **slice-to-slice** continuity, maintaining volumetric coherence with modest parameter cost.